


Article

Thermochemical Analysis of Hydrogenation of Pd-Containing Composite Based on TiZrVNbTa High-Entropy Alloy

Ivan Savvotin ¹, Elena Berdonosova ¹, Artem Korol ², Vladislav Zadorozhnyy ^{2,*}, Mikhail Zadorozhnyy ^{2,3} , Evgeniy Statnik ², Alexander Korsunsky ² , Mikhail Serov ⁴ and Semen Klyamkin ¹ 

- ¹ Department of Chemistry, Lomonosov Moscow State University, 119991 Moscow, Russia; 79166550606@mail.ru (I.S.); ellenganich@highp.chem.msu.ru (E.B.); klyamkin@highp.chem.msu.ru (S.K.)
² Accelerated Particle Laboratory, National University of Science and Technology MISIS, Leninskiy Prospekt 4, 119049 Moscow, Russia; artemkorol1998@gmail.com (A.K.); zadorozhnyy.m.yu@mail.ru (M.Z.); statnik.es@misis.ru (E.S.); a.korsunskii@misis.ru (A.K.)
³ Center for Project Activities, Moscow Polytechnic University, Bolshaya Semenovskaya St., 2, 107023 Moscow, Russia
⁴ Moscow Aviation Institute, National Research University, 119049 Moscow, Russia; serovrmf@yandex.ru
* Correspondence: vuz@misis.ru

Abstract: The microcalorimetric hydrogen titration technique combined with conventional volumetric measurements has been used to reveal peculiarities of the hydrogenation of the single-phase TiZrVNbTa equiatomic high-entropy alloy. The alloy has been produced in the form of microfibers by the pendent drop melt extraction technique. Palladium coating of the fibers has been applied to enable first hydrogenation at room temperature without additional activation. An analysis of the obtained data allows us to evaluate the dependence of hydrogenation enthalpy on the hydrogen concentration in the alloy. Three concentration ranges, presumably related to the formation of the hydrogen solid solution, monohydride and dihydride phases, have been identified, and the corresponding ΔH values of about -100 , -80 and -60 kJ/mol H_2 , respectively, have been determined.

Keywords: hydrogen storage; high-entropy alloys; calorimetry; palladium coating



Citation: Savvotin, I.; Berdonosova, E.; Korol, A.; Zadorozhnyy, V.; Zadorozhnyy, M.; Statnik, E.; Korsunsky, A.; Serov, M.; Klyamkin, S. Thermochemical Analysis of Hydrogenation of Pd-Containing Composite Based on TiZrVNbTa High-Entropy Alloy. *Appl. Sci.* **2023**, *13*, 9052. <https://doi.org/10.3390/app13169052>

Academic Editor: Victor Franco Correia

Received: 31 May 2023

Revised: 27 July 2023

Accepted: 6 August 2023

Published: 8 August 2023



Copyright: © 2023 by the authors. Licensee MDPI, Basel, Switzerland. This article is an open access article distributed under the terms and conditions of the Creative Commons Attribution (CC BY) license (<https://creativecommons.org/licenses/by/4.0/>).

1. Introduction

All of the world's leading countries have been paying great attention to the development of alternative (renewable) energy sources in recent years. Hydrogen is considered as one of the most promising fuels with a high energy capacity. However, for widespread use, it is necessary to solve many problems, such as separation of hydrogen from gas mixtures, compact storage and recycling for energy production.

High-entropy alloys (HEAs) formed by five or more metals with close to equiatomic concentrations [1] can be used to overcome these problems. These alloys have a high hardness [2], corrosion resistance [3,4], wear resistance and thermal stability. Some of them show a high hydrogen sorption capacity [5] because of strong deformation of the HEAs' crystal lattice due to the difference in atomic sizes, which creates additional opportunities for hydride formation. For example, the equiatomic alloy TiVZrNbHf absorbs a large amount of hydrogen ($H/M = 2.5$, which exceeds the hydrogen absorption capacity of any of the alloy elements) [6]. Such a high H/M ratio is not typical for transition metals, except for very high pressures ($TiH_{1.8} + \gamma$ at 5 GPa [7]).

In order to predict and adjust HEAs' properties, it is customary to consider parameters such as the VEC (concentration of valence electrons), δ (parameter characterizing difference in atomic sizes of elements in an alloy), δ_x (parameter characterizing the difference in electronegativity of elements in an alloy), ΔH_{mix} (enthalpy of mixing of alloy components) and Ω (parameter relating to the melting point (T_m), ΔH_{mix} and ΔS_{mix}) [8,9].

Two trends correlating with the VEC were found experimentally: first, the volume expansion per metal unit (α) increases linearly with increasing the VEC; second, the

beginning of the hydrogen desorption temperature decreases linearly with increasing the VEC, and it reaches room temperature at VEC = 6.4 [8].

The calculation of various thermodynamic parameters of alloys makes it possible to predict the formation of single-phase structures, to evaluate the hydrogen absorption properties of alloys. As it has been shown in [10], at $\Omega < 1$, large values of ΔH_{mix} determine the predominant contribution of the enthalpy factor to the free energy change (ΔG), which contributes to the formation of highly stable binary and ternary intermetallic compounds. At $\Omega > 1$, the entropy contribution prevails and there is a tendency for the formation of disordered solid solutions. It is possible to construct phase stability diagrams based on the calculations, but the limiting factor of the phase formation and stability prediction method is related to its inability to take into account all competing phases [11]. Compared to the empirical approach, thermodynamic models have much greater accuracy and were able to determine the composition areas in which single-phase HEAs exist [11–14].

The CALPHAD (CALculation of PHase Diagrams) is another method for calculating the composition of stable phases in studies of wind farms for hydrogen storage [15,16]. The construction of phase diagrams of equilibrium phases is based on the use of thermodynamic models that analytically estimate the Gibbs–Helmholtz free energy for all expected competing phases [17]. At the moment, several promising HEA systems for hydrogen storage have been discovered using the CALPHAD method [18–20], for example, the Ti–V–Zr–Nb–Hf alloy. The CALPHAD method has such disadvantages as limiting the prediction possibilities outside the ranges approximated by polynomial functions, errors introduced by the lack of data on competing intermetallic phases and limitations in predicting metastable phases (which may be the most successful).

Conventional arc melting is the most common and the simplest method for the synthesis of HEAs. However, because of the high chemical activity of the components and their surface oxidation in air hydrogen, interaction is limited. Activation of those alloys requires preliminary high-temperature (573–973 K) treatment [9,21]. During the activation, the partial reduction of surface oxides, the formation of cracks and defects (dislocations, grain boundaries, violations of atomic packing) occur. The combination of these processes contributes to hydride formation [22,23]. The key factors affecting activation parameters of HEAs are the valence state of surface atoms and the difference in the atomic sizes of constituting alloy elements [24].

In some cases, for example, for the arc-melted TiZrNbCrFeNi alloy with the C14 Laves phase structure, hydrogen absorption (up to 1.5 wt.%) at room temperature is observed without preliminary activation. However, desorption is possible only at 473 K; the reversible capacity does not exceed 1.1 wt.%. This is due to the formation of two phases, one of which is less active to accommodate hydrogen atoms [25]. The Ti–Zr–V–Cr–Ni alloy with a similar crystal structure demonstrates a higher reversible hydrogen sorption capacity (1.5 wt.%) and better cyclic stability, which indicates the future potential of developing this class of high entropy intermetallic-based materials for hydrogen storage [26].

Sometimes, during the formation of a hydride, the initial single-phase HEA transforms into a hydride consisting of several phases, which is probably determined by the elemental composition of the initial HEA. However, no general patterns can be traced in this case. It was found that, in addition to the main FCC phase, the tantalum-containing hydrides contain an additional BCT phase: 30.3 wt.% in TiVNbTaH_x, 24.2 wt.% in TiVZr_{0.15}NbTa_{0.85}H_x, 8.2 wt.% in TiVZr_{0.5}NbTa_{0.5}H_x and 2.2 wt.% in TiVZr_{0.74}NbTa_{0.26}H_x [27].

It has been shown that HEAs with a high content of 8–10 group (Fe, Co, Ni) metals tend to keep the initial C14 crystalline structure in their hydrides, while the volume of the unit cell can significantly increase with an almost unchanged ratio of c/a (for ZrTiVCrFeNi, the volumetric effect of hydride formation is 23.3% for an untreated alloy and 2.4% for a heat-treated alloy [28]).

Mg-containing alloys tend to form hydrides with an FCC crystal structure; for example, BCC–HEA MgZrTiFe_{0.5}Co_{0.5}Ni_{0.5} absorbs hydrogen in two stages: first, a solid solution with a BCC structure is formed, in which hydrogen occupies octahedral positions, and

then the solid solution turns into a hydride with an FCC lattice, in which hydrogen atoms occupy tetrahedral positions [18].

Group 5 metals (V, Nb, Ta) with a bcc crystal structure have a high hydrogen permeability and are promising materials for membrane hydrogen separation [29,30]. However, in most cases, individual metals are subjected to hydrogen embrittlement and passivation, which hinders their industrial use [31]. Nowadays, many works on developing HEA-based membranes whose properties will be superior to traditional Pd-based alloys are in progress. For example, at 673 K, the multicomponent Nb₄₀Ti₁₈Zr₁₂Ni₂₅Co₅ alloy has demonstrated a higher ($3.8 \times 10^{-8} \text{ mol H}_2 \cdot \text{m}^{-1} \cdot \text{s}^{-1} \cdot \text{Pa}^{-0.5}$) permeability than the conventional Pd_{0.23}Ag_{0.77} ($1.6 \times 10^{-8} \text{ mol H}_2 \cdot \text{m}^{-1} \cdot \text{s}^{-1} \cdot \text{Pa}^{-0.5}$) [32].

The thermochemical parameters of the interaction in metal-hydrogen systems are essential both for understanding the mechanism of hydrogen absorption and transport, and for practical application. For some HEAs, the enthalpy of hydride formation has been calculated on the basis of experimentally measured hydrogen absorption isotherms using the Van 't Hoff equation. For alloys with bcc structure TiVZrNb ($a = 3.3047 \text{ \AA}$), TiVZrNbHf ($a = 3.3664 \text{ \AA}$) and TiV_{0.5}ZrNbHf ($a = 3.3911 \text{ \AA}$), the enthalpy of hydrogen absorption decreases in absolute value with increasing the cell parameter from 67.6 to 61.8–59.1 kJ/mol H₂ [8]. This trend is the opposite of that observed for other types of metal hydrides (AB, AB₂ and AB₅) where the hydride stability (that is the formation enthalpy) increases with an increase in the interstitial void size [33–35]. The reported data on the enthalpy of hydride formation are of particular interest considering some well-known metal-hydrogen systems with similar equilibrium hydrogen absorption pressure, but a higher enthalpy of hydrogenation (for example, -75 kJ/mol H_2 for MgH₂, [36]).

In addition to the conventional analysis of pressure-composition isotherms (PCI) by means of the Van 't Hoff equation, calorimetric studies can provide some useful items of information on the hydrogenation behavior of alloys. Calorimetric measurements directly give the values of the enthalpy of the process at a certain fixed temperature at all its stages, and not only in the region of the phase transition. This is of special importance in the case when there are no clear boundaries of the phase regions on the isotherms. The effectiveness of such a thermochemical analysis of metal-hydrogen systems, the so-called calorimetric titration, has been demonstrated in [37,38], including for disordered alloys.

The need for high-temperature activation seriously complicates the use of this experimental research technique. We have proposed the deposition of a thin palladium layer at the alloy surface in order to eliminate the high-temperature pre-treatment stage and ensure the hydrogen interaction with the HEA at room temperature. Palladium coating is a known approach to improving different characteristics of alloys in the reaction with hydrogen. It was found for the AB₅ alloy ($A = \text{La}_{0.34}\text{Ce}_{0.50}(\text{Pr,Nd})_{0.16}$; $B = \text{Ni}_{0.63}\text{Co}_{0.13}\text{Mn}_{0.12}\text{Al}_{0.12}$) that surface modification with palladium produced by electrodeposition from the solution greatly improves the activation characteristics and the resistance to poisoning at the interaction with hydrogen. In particular, the hydrogen absorption rate after prolonged exposure to air increases about 100 times for surface-modified materials compared to the unmodified alloy [22]. Also, an increase in the rate of hydrogen uptake and easier activation after the palladium coating has been observed for TiFe-based alloys [39] and TiMn_{1.52} [40].

In this work, the hydrogen absorption properties of EBM-PDME (electron beam melting with pendent drop melt extraction) TiZrVNbTa fibers with a palladium surface coating were studied. This crucible-less processing mode is suitable for materials with a high melting point [41,42]. Due to the high (up to 10^6 K/s) cooling rates, microcrystalline and amorphous materials can be obtained. The absorption isotherm for the first cycle has been measured at room temperature without any preliminary activation; the maximum sorption capacity was 1.7 wt.%. The enthalpy of absorption in a wide range of hydrogen concentrations has been evaluated using Tian–Calvet calorimetry. The data obtained allows us to suggest the prospects of the proposed approach to a deeper study of the processes of hydride formation in HEAs.

2. Materials and Methods

2.1. Alloy and Fiber Preparation

The alloy $\text{Ti}_{20}\text{Zr}_{20}\text{V}_{20}\text{Nb}_{20}\text{Ta}_{20}$ was chosen based on previously published data [43]. Zr (purity 99.5%), Ti (purity 99.5%), V (purity 99.7%), Nb (purity 99.95%) and Ta (purity 99.95%) metal chips were used to prepare powder mixtures and ingots. Ti–Zr–V–Nb–Ta alloy ingots (in equiatomic elemental composition) were produced by the arc melting of mixtures of pure metals in an argon atmosphere purified with a Ti getter. The ingots were turned over and remelted five times to ensure the homogeneity of the composition after melting.

The method of EBM-PDME was used to obtain micro-sized fibers from the arc-melted ingot [43,44]. The formation of fibers was carried out in a vacuum installation with an electron beam melting of the previously melting material synthesized by conventional arc. According to this method, the lower end of the vertically positioned workpiece melts to form a hanging drop of melt. The resulting drop is fed to a rotating heat absorber and, after solidification, is cut into an isosceles triangle. As the heat sink rotates, the solidified material is removed from the melt in the form of fibers under the action of centrifugal force.

2.2. Palladium Coating Obtaining

The palladium coating was deposited using a laboratory SPI Module Sputter Coater, SPI[®], USA. A metal plate (Pd 99.99%) of a diameter of 60 mm and a thickness of 0.5 mm served as a source of palladium. After loading the HEA sample, the chamber was evacuated for 5 min to a pressure of about 0.01 Pa. Sputtering was carried out in an Ar (99.99%) atmosphere.

For palladium deposition, the sputtered sample was placed at approximately 5 cm from the palladium source. The application time was 60 s, while after 30 s, the sample was turned over to ensure complete coverage of the surface of the fibers. The coating thickness can be estimated using the following equation:

$$d = KIUt \quad (1)$$

where d is the coating thickness, Å; K is a constant depending on the sprayed material and the distance from the target to the sample (for Pd and 50 mm $K \approx 2.5$); I is the plasma current strength, mA; and U is the applied voltage, kV.

The deposition was carried out at current $I = 30$ mA and voltage $U = 1$ kV. In order to detect and measure such a thin Pd layer, a protected Pt layer was deposited onto the specimen surface by the GIS system inside FIB-SEM Tescan Solaris using the following parameters: ion deposition mode, beam current of 150 pA, beam landing energy of 30 kV, thickness of 2 µm, width of 2 µm and length of 10 µm. The cross-section of the material was etched via ion beam with 30 kV and 2.5 nA, with a subsequent polishing using ion beam with 30 kV and 250 pA.

2.3. Hydrogen Sorption Properties

The study of the hydrogen sorption properties of the HEAs was carried out by the volumetric and calorimetric methods using a heat-conducting differential microcalorimeter of the Tian-Calvet type (DAC-1 a) combined with a hand-made Sieverts measuring system [45]. In this experimental technique, the heat flow accompanying the hydrogen absorption process is recorded simultaneously with stepwise isotherm measuring. For dehydrogenation, the samples were subjected to degassing at 673 K in a dynamic vacuum of 1 Pa for 10 h.

2.4. Scanning Electron Microscopy and Energy Dispersive X-ray Spectroscopy

The study of the morphology of materials was carried out on a high-resolution scanning electron microscope (SEM) TESCAN Vega3 XM and FIB-SEM TESCAN Amber with Ga⁺ ions (TESCAN ORSAY HOLDING, Brno, Czech Republic). A quantitative elemental analysis was performed using an Oxford Instruments INCA x-act energy dispersive microanalyzer (Oxford Instruments, High Wycombe, UK).

In order to detect and measure such a thin Pd layer, a protected Pt layer was deposited onto the specimen surface by the GIS system inside FIB-SEM Tescan Solaris using the following parameters: ion deposition mode, beam current of 150 pA, beam landing energy of 30 kV, thickness of 2 μm , width of 2 μm and length of 10 μm . The cross-section of the material was etched via ion beam with 30 kV and 2.5 nA, with a subsequent polishing using ion beam with 30 kV and 250 pA.

2.5. X-ray Phase Analysis

X-ray diffraction patterns of the samples were obtained at room temperature on a Thermo ARL X'TRA powder diffractometer with $\text{CuK}\alpha$ radiation ($\lambda = 1.5405\text{\AA}$, reflection geometry, semiconductor Peltier detector, with angles 2θ in the range from 10° to 120° at a speed of $0.5^\circ/\text{min}$). All calculations were performed using the PHAN% software [46]. To calculate the lattice parameter, the Rietveld refinement was used.

2.6. Time-of-Flight Secondary Ion Mass Spectrometry

In order to reliably confirm the thickness and composition of Pd coating, Time-of-Flight Secondary Ion Mass Spectrometry (TOF-SIMS) was applied in combination with the above-described FIB-SEM. The principle of this method is based on stepwise secondary ion extraction from the specimen surface by etching it with FIB. This allows us to obtain the 3D ions' distributions considering the homogeneous layer-by-layer etching that requires some FIB calibration procedures. In this study, TOF-SIMS measurements were performed under the following conditions: ion beam voltage of 30 kV, ion beam current of 250 pA (to obtain gentle etching with a small penetration depth), positive ion polarity, dwell time of 20 μs , resolution of 1024×1024 pixels and view field of 20 μm .

3. Results and Discussion

The alloy studied in this work has been produced by arc melting followed by EBM-PDME processing. The composition of the alloy was analyzed by the EDX method (Table 1).

Table 1. Chemical composition of TiZrVNbTa after EBM-PDME.

Element	Set Composition, at. %	Defined Composition, at. %
Ti	20	18.1
Zr	20	19.7
V	20	19.2
Nb	20	21.5
Ta	20	21.5

It is confirmed that the chemical composition of the resulting alloy is close to the initially specified nominal composition.

3.1. Palladium Coating

The thickness of the palladium coating, defined by FIB-SEM, is ≈ 240 nm (Figure 1), and the mass fraction of Pd is at the level of 0.01%.

The EDX analysis was used to confirm the progress of the palladium deposition process. The presence of palladium on the surface of the HEA fibers was established (Figure 2); however, the SEM resolution used does not allow us to characterize the morphology of a very thin formed coating. The TOF-SIMS was used to analyze the chemical composition of the deposited layer which allowed us to conclude that the process of deposition was carried out. The obtained Pd^+ ions' distribution after TOF-SIMS measurements is shown in Figure 2d. In order to estimate the depth of the Pd coating, this map was averaged across the x -axis as illustrated in Figure 2e. It was confirmed that the Pd coating is quite homogenous and has the same thickness of ~ 240 nm.

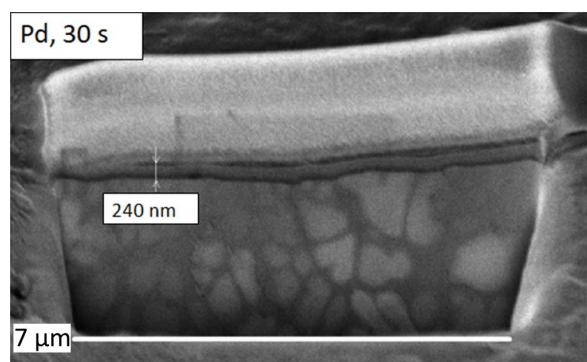


Figure 1. SEM image visualizing thickness of the palladium coating.

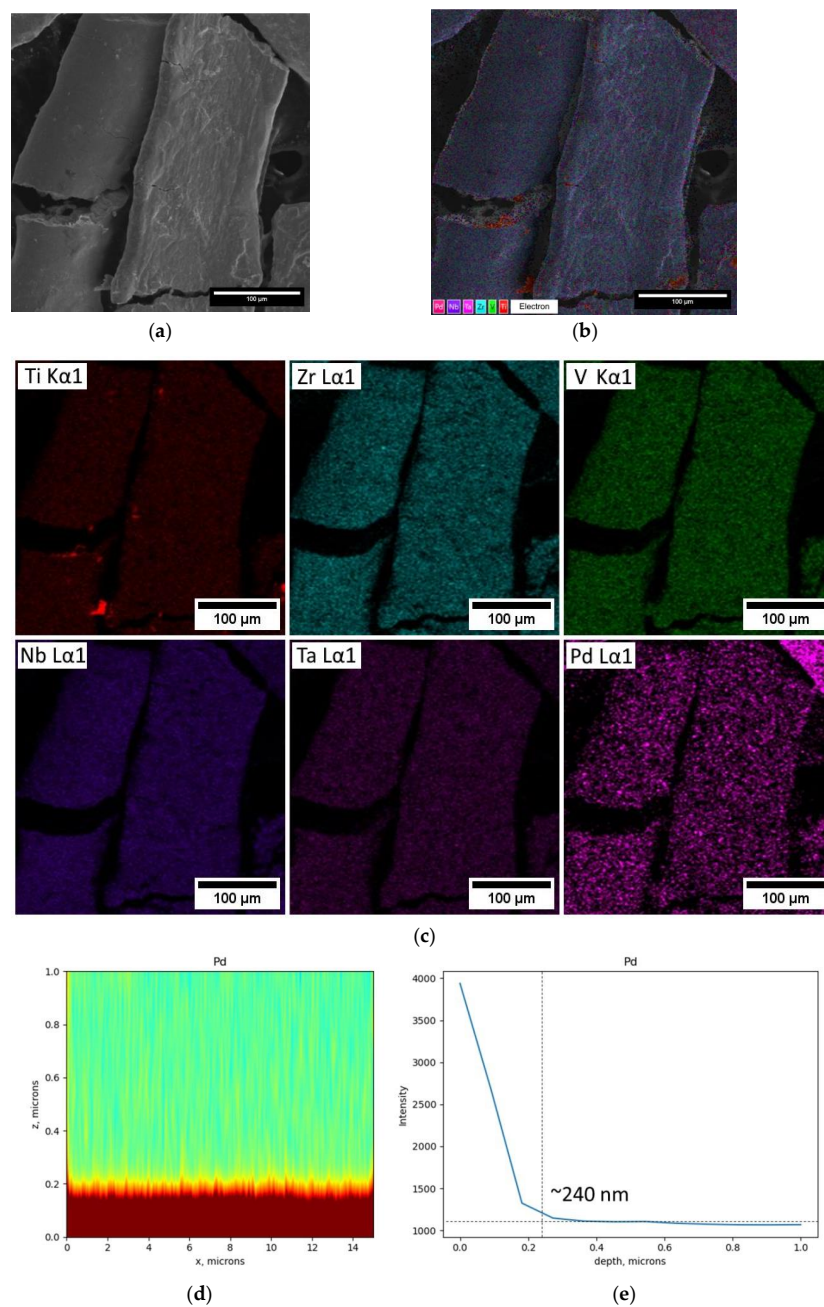


Figure 2. SEM images of (a) palladium-coated TiZrVNbTa fibers; (b) multilayer EDX image; (c) element mapping; (d) thickness distribution of Pd (red); (e) signal intensity dependence on thickness of Pd.

According to the XRD analysis, the alloy obtained by EBM-PDME is single-phase (Figure 3a) with a bcc lattice (Table 2). We have to note that the palladium coating does not affect the XRD patterns; the palladium phase is not detected because of its very small amount. The unit cell parameter of the alloy is 0.3301 nm, which agrees with the literature data on the similar alloy (0.3304 nm [2]).

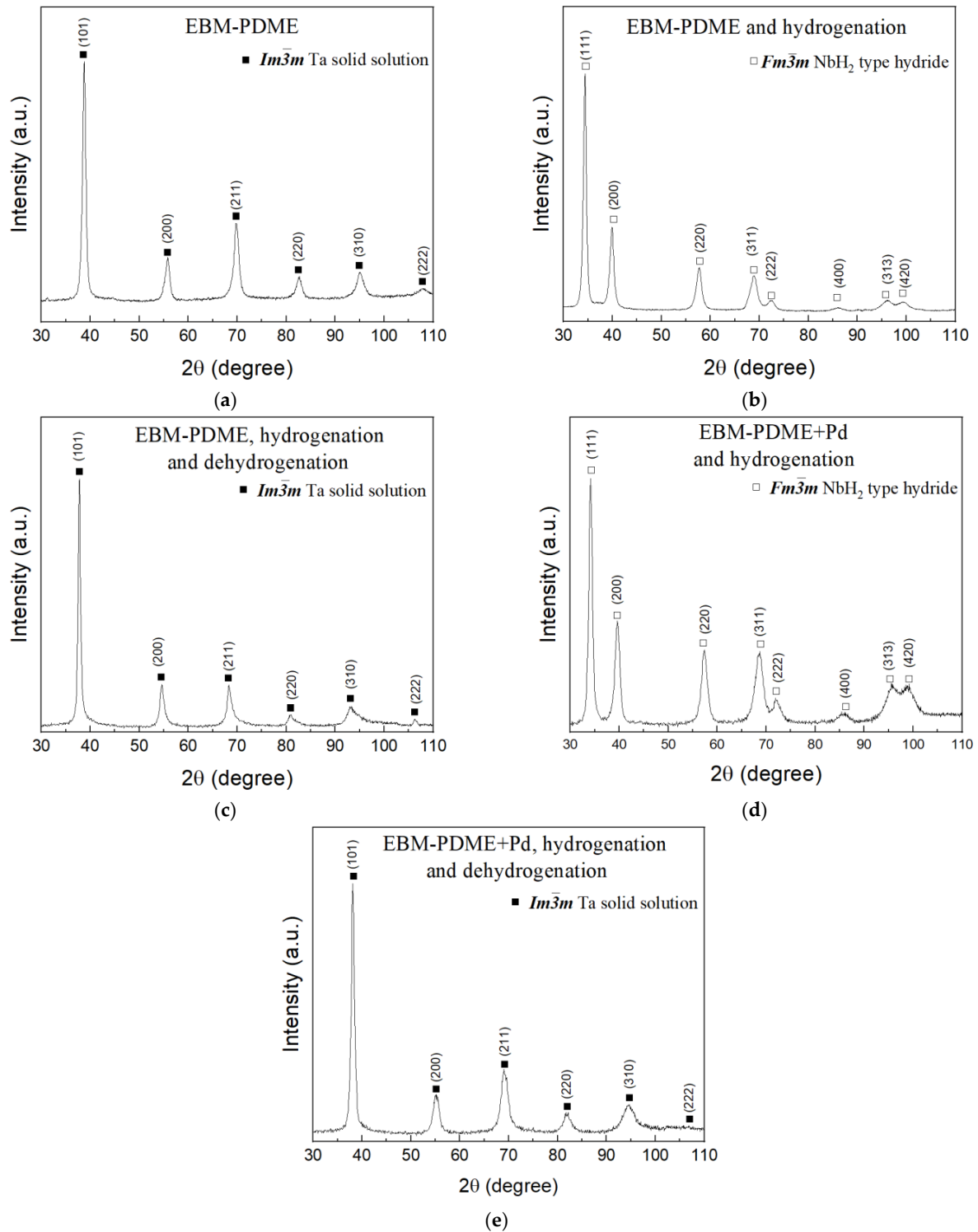


Figure 3. X-ray diffraction patterns of the EBM-PDME fibers TiZrVNbTa alloy obtained by: (a) as prepared; (b) after hydrogenation; (c) after dehydrogenation; (d) palladium-coated fibers after hydrogenation; (e) palladium-coated fibers after dehydrogenation.

Table 2. Phase composition and structure parameters of the EBM-PDME TiZrVNbTa alloy.

Sample	Space Group	Phase Content, %	Unit Cell Parameters, nm	Crystallite Size, nm	V, nm ³	ΔV/V ₀
As prepared						
TiZrVNbTa	Im $\bar{3}$ m	100	a = 0.3301(5)	>200	0.0359(3)	-
After hydrogenation						
TiZrVNbTa	Fm $\bar{3}$ m	100	a = 0.4539(3)	>200	0.0935(2)	30.2
Pd@TiZrVNbTa	Fm $\bar{3}$ m	100	a = 0.4538(1)	>200	0.0935(1)	30.2
TiZrVNbTa *	Fm $\bar{3}$ m	95	a = 0.4517(5)	>200	0.0922(4)	27.3
			a = 0.4795(7)			
	Pnnn	5	b = 0.4829(4) c = 0.3450(2)	>200	0.0799(3)	22.1
After dehydrogenation						
TiZrVNbTa	Im $\bar{3}$ m	100	a = 0.3321(2)	100	0.0366(6)	1.9
Pd@TiZrVNbTa	Im $\bar{3}$ m	100	a = 0.3314(4)	100	0.0364(2)	1.4
TiZrVNbTa *	Im $\bar{3}$ m	95	a = 0.3304(2)	40	0.0361(5)	0.6
	Im $\bar{3}$ m	5	a = 0.3395(7)	50	0.0391(2)	8.2

*—arc-melted alloy [27].

3.2. Hydrogen Sorption Properties

Volumetric measurements were carried out in a wide range of pressures and temperatures to evaluate the hydrogen sorption capacity of the TiZrVNbTa alloy. Since the original Pd-free fibers do not react with hydrogen at room temperature without preliminary activation, they were subjected to heating in a vacuum (1 Pa) for 2 h at 673 K. Then, the reactor was filled with hydrogen at a pressure of 40 bar at the same temperature. The maximum value of the absorbed hydrogen reached 1.6 wt.% (H/M = 1.5). It is worth noting that, under the conditions described above, we were not able to measure the absorption isotherm step by step. Moreover, the subsequent hydrogen desorption was not complete: the re-hydrogenation, although it proceeds at room temperature, shows a noticeably smaller capacity of about 1.25 H/M. Only a separate long-term degassing at a temperature of 673 K for 10 h allowed us to remove the maximum possible amount of hydrogen and to characterize the products of such dehydrogenation.

The XRD analysis of the hydrogenation products (Table 2) indicates that the main phase is the fcc hydride (space group Fm $\bar{3}$ m). The transformation of bcc to fcc is complete; no additional phases were found. The volume expansion after hydride formation was 30.2%, which is 18% per 1 H atom. This value is slightly higher compared to literature data for related TiVZrNbTa alloys (14%) [47].

After prolonged dehydrogenation, the transition from the fcc to the original bcc structure has been recorded. Compared to the initial alloy, the unit cell parameter increases after dehydrogenation, which corresponds to the formation of a solid solution phase with a volume expansion of 1.9%. Assuming a linear dependence of the volume expansion on the hydrogen concentration, the residual hydrogen content is about 0.1 H/M.

The applied palladium coating dramatically increases the activity of the alloy in relation to hydrogen. Already, the first hydrogenation proceeds at room temperature without any additional activation and without a noticeable induction period. The recorded hydrogen absorption isotherm for Pd@TiZrVNbTa microfibers is shown in Figure 4. We note the absence of a clear plateau on the isotherm, which would allow us to distinguish individual phase transformations as the amount of absorbed hydrogen increases.

The maximum hydrogen sorption capacity was 1.7 H/M (1.8 wt.%), which is slightly more than for palladium-free fibers. According to the XRD results (Figure 3d, Table 2), a single-phase product is formed with the same unit cell volume expansion as for the original alloy (30.2%). Comparing the resulting isotherm with an isotherm of the second cycle for the palladium-free alloy (Figure 4), there is a significant increase in absorption pressure. This phenomenon is often observed in metal hydride systems, and it may be associated

with the necessity to overcome the energy barrier to initiate the primary act of interaction of an alloy with hydrogen.

The desorption under the conditions described above leads to the reverse phase transition from fcc to the original bcc cell, similar to that observed for the non-coated alloy. Yet, the residual unit cell parameter ($\Delta V/V_0$) = 1.4% indicates a more complete dehydrogenation process due to a certain catalytic effect of palladium during dehydrogenation.

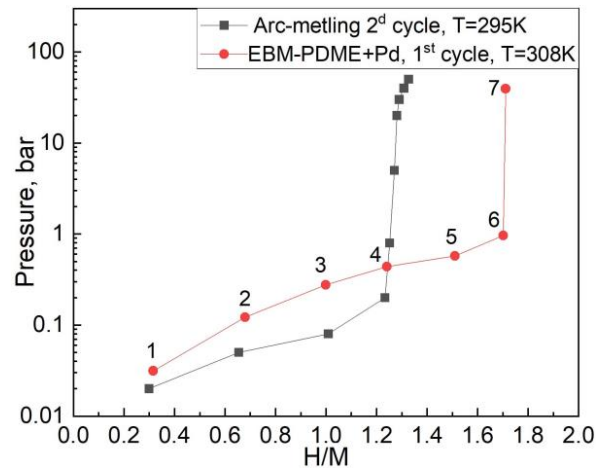


Figure 4. Hydrogen absorption isotherms of the $TiZrVNbTa$ alloy.

3.3. Calorimetric Tests

As it is mentioned above, the palladium coating enables the low-temperature first hydrogenation, which allowed us to perform a correct calorimetric study of this process. At the initial stage of the reaction (hydrogen concentration in the metallic phase of 0 to 0.7 H/M), the maximum heat release close to 100 kJ/mol H_2 in absolute value has been recorded (Figure 5), which corresponds to the equilibrium pressure range of 0.03–0.1 bar at 308 K (Figure 4). As the reaction proceeds, the heat release gradually decreases to 80 kJ/mol H_2 . In the hydrogen concentration range from 1 to 1.5 H/M, one can observe a constant value of the reaction enthalpy of 60 kJ/mol H_2 . Most likely, this corresponds to the phase transformation of a monohydride to dihydride phase, similarly described in [9]. When the phase transition is completed, the thermal effect of the reaction reduces sharply to 40 kJ/mol H_2 .

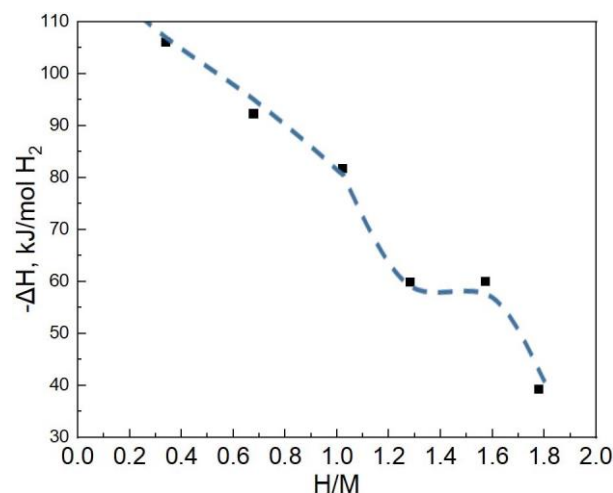


Figure 5. Concentration dependence of the enthalpy of hydrogen absorption by $Pd@TiZrVNbTa$; $T = 308$ K.

The analysis of experimental heat release curves (Figure 6) provides some important additional items of information.

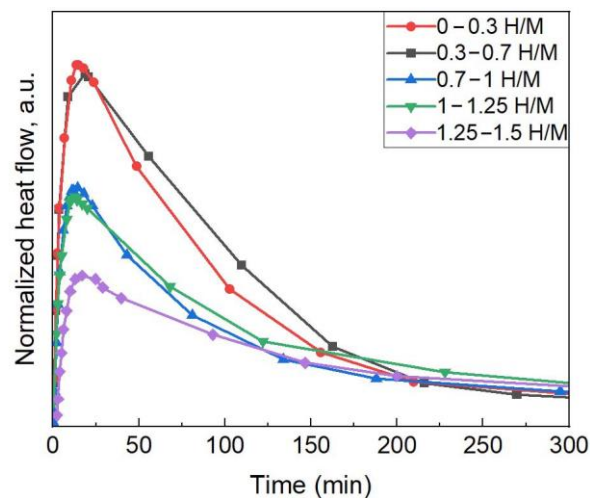


Figure 6. Normalized heat flow curves for a different hydrogen concentration range.

First, we point out the absence of any induction period for all curves corresponding to different concentration ranges. Second, there is an acceleration section on each curve, and in all cases, the maximum heat release rate is reached after 15–17 min, regardless of the concentration range and the overall thermal effect on each section. This peculiarity is not related to the inertia of the measuring system, the response time of which is at the level of several seconds. The nature of the phenomenon is not entirely clear. It is quite likely that it is related to the features of the crystallite structure of the alloy under test and the time to reach the maximum heat release rate (i.e., the maximum reaction rate) is determined by the characteristic migration path of hydrogen in the metal lattice. Third, all experimental heat release curves can be conditionally divided into three groups depending on the concentration range described by them (Figure 6). Each of these groups corresponds to processes similar in nature and thermochemical characteristics. The concentration ranges 0–0.3 and 0.3–0.7 are characterized by the maximum heat release rate, and the curves practically coincide. Based on the general concepts of phase transformations in metal-hydrogen systems, this concentration range may correspond to the formation of a solid solution in an HEA matrix. In the range of 0.7–1.25 H/M, the formation of a monohydride phase occurs, and at higher concentrations, this monohydride turns into a dihydride. Probably, the boundaries of these concentration ranges require further clarification, although the very fact of their separation is quite clearly seen from the results of the thermochemical analysis.

4. Conclusions

The single-phase high-entropy alloy (HEA) TiZrVNbTa with an equiatomic element concentration has been obtained in the form of microfibers using electron beam melting combined with pendant drop melt extraction. The structure study of the alloy in the course of the interaction with hydrogen has shown that a reversible phase transformation from the initial bcc HEA to fcc-type hydride occurs during hydrogenation.

Palladium coatings on HEA fibers allowed us to eliminate the stage of the high-temperature activating treatment, and to perform the complete hydrogenation at room temperature. The maximum hydrogen absorption capacity of 1.7 H/M was reached.

The values of the enthalpy of hydrogen adsorption in a wide range of concentrations were obtained using Tian–Calvet calorimetry. The enthalpy of absorption has a strong dependence on the composition of the hydride phase, which may indicate a multi-stage mechanism of the phase transformation. Three concentration ranges with hydrogenation

enthalpy, a ΔH of about -100 , -80 and -60 kJ/mol, can be attributed to the formation of the hydrogen solid solution, monohydride and dihydride phases, respectively.

The obtained results demonstrate that the used calorimetric titration technique is a powerful tool for in-depth study of hydrogenation processes in complex metal hydride systems, including high-entropy alloys.

Author Contributions: Methodology, E.S.; formal analysis, M.Z.; investigation, M.S. and E.B.; data curation, A.K. (Alexander Korsunsky); writing—original draft preparation, I.S.; writing—review and editing, V.Z.; project administration, S.K. and A.K. (Artem Korol). All authors have read and agreed to the published version of the manuscript.

Funding: The research was supported by the Ministry of Science and Higher Education of the Russian Federation, projects №AAAA-A16-116053110012-5, 122012400186-9 and grant № K1-2022-032 in the framework of the Competitiveness Improvement Program of NUST MISIS. M.Z. acknowledges the financial support from the Moscow Polytechnic University within the framework of the grant named after Pyotr Kapitsa.

Institutional Review Board Statement: Not applicable.

Informed Consent Statement: Not applicable.

Data Availability Statement: The data presented in this study are available on request from the corresponding author.

Conflicts of Interest: The authors declare no conflict of interest.

References

1. Yang, F.; Wang, J.; Zhang, Y.; Wu, Z.; Zhang, Z.; Zhao, F.; Huot, J.; Jasmina, G.; Nikola, N. Recent progress on the development of high entropy alloys (HEAs) for solid hydrogen storage: A review. *Int. J. Hydrogen Energy* **2022**, *47*, 11236–11249. [\[CrossRef\]](#)
2. Gorban, V.; Shaginyan, R.; Krapivka, N.; Firstov, S. Superhard vacuum coatings based on high-entropy alloys. *Powder Met. Met. Ceram.* **2016**, *54*, 725–730. [\[CrossRef\]](#)
3. Zhang, G.; Ming, K.; Kang, J.; Huang, Q.; Zhang, Z.; Zheng, X.; Bi, X. High entropy alloy as a highly active and stable electrocatalyst for hydrogen evolution reaction. *Electrochim. Acta* **2018**, *279*, 19–23. [\[CrossRef\]](#)
4. Ma, P.; Zhao, M.; Zhang, L.; Wang, H.; Gu, J.; Sun, Y.; Ji, W.; Fu, Z. Self-supported high-entropy alloy electrocatalyst for highly efficient H_2 evolution in acid condition. *J. Mater.* **2020**, *6*, 736–742. [\[CrossRef\]](#)
5. Yadav, T.; Kumar, A.; Kumar, S.; Krishna, N. High-Entropy Alloys for Solid Hydrogen Storage: Potentials and Prospects. *Proc. Indian Natl. Sci. Acad.* **2022**, *7*, 147–156. [\[CrossRef\]](#)
6. Sahlberg, M.; Karlsson, D.; Zlotea, C.; Jansson, U. Superior hydrogen storage in high entropy alloys. *Sci. Rep.* **2016**, *6*, 36770. [\[CrossRef\]](#)
7. Nakamura, K.; Fukai, Y. High-pressure studies of high-concentration phases of the TiH system. *J. Alloys Compd.* **1995**, *231*, 46–50. [\[CrossRef\]](#)
8. Ek, G.; Nygård, M.; Pavan, A.; Montero, J.; Henry, P.; Sørby, M.; Witman, M.; Stavila, V.; Zlotea, C.; Hauback, B.; et al. Elucidating the effects of the composition on hydrogen sorption in TiVZrNbHf-based high-entropy alloys. *Inorg. Chem.* **2020**, *60*, 1124–1132. [\[CrossRef\]](#)
9. Marques, F.; Balcerzak, M.; Winkelmann, F.; Zepon, G.; Felderhoff, M. Review and outlook on high-entropy alloys for hydrogen storage. *Energy Environ. Sci.* **2021**, *14*, 5191–5227. [\[CrossRef\]](#)
10. Yang, X.; Zhang, Y. Prediction of high-entropy stabilized solid-solution in multi-component alloys. *Mater. Chem. Phys.* **2012**, *132*, 233–238. [\[CrossRef\]](#)
11. George, E.; Raabe, D.; Ritchie, R. High-entropy alloys. *Nat. Rev. Mater.* **2019**, *4*, 515–534. [\[CrossRef\]](#)
12. Troparevsky, M.; Morris, J.; Kent, P.; Lupini, A.; Stocks, G. Criteria for Predicting the Formation of Single-Phase High-Entropy Alloys. *Phys. Rev. X* **2015**, *5*, 011041. [\[CrossRef\]](#)
13. Troparevsky, M.; Morris, J.; Daene, M.; Wang, Y.; Lupini, A.; Stocks, G. Beyond Atomic Sizes and Hume-Rothery Rules: Understanding and Predicting High-Entropy Alloys. *JOM* **2015**, *67*, 2350–2363. [\[CrossRef\]](#)
14. King, D.; Middleburgh, S.; McGregor, A.; Cortie, M. Predicting the formation and stability of single phase high-entropy alloys. *Acta Mater.* **2016**, *104*, 172–179. [\[CrossRef\]](#)
15. Edalati, K.; Li, H.; Kilmametov, A.; Floriano, R.; Borchers, C. High-pressure torsion for synthesis of high-entropy alloys. *Metals* **2021**, *11*, 1263. [\[CrossRef\]](#)
16. Floriano, R.; Zepon, G.; Edalati, K.; Fontana, G.; Mohammadi, A.; Ma, Z.; Contieri, R. Hydrogen storage in TiZrNbFeNi high entropy alloys, designed by thermodynamic calculations. *Int. J. Hydrogen Energy* **2020**, *45*, 33759–33770. [\[CrossRef\]](#)
17. Sobko, M.; Lushnikov, S.; Verbetsky, V.; Agafonov, S. Structure of $(ZrTi)_{0.5}(VCrFe(Ni_{0.9}Cu_{0.1}))_{0.5}$ - and $(ZrTi)_{0.5}(VMoFeNi)_{0.5}$ -Based Deuterides. *Inorg. Mater.* **2020**, *56*, 1106–1112. [\[CrossRef\]](#)

18. Zepon, G.; Leiva, D.; Strozi, R.; Bedoch, A.; Figueroa, S.; Ishikawa, T.; Botta, W. Hydrogen-induced phase transition of $\text{MgZrTiFe}_{0.5}\text{Co}_{0.5}\text{Ni}_{0.5}$ high entropy alloy. *Int. J. Hydrogen Energy* **2018**, *43*, 1702–1708. [\[CrossRef\]](#)
19. Xu, Y.; Lyu, Y.; Liu, H.; Pan, X.; Lu, T.; Zhu, T.; Luo, G. Hydrogen isotope permeation and retention behavior in the CoCrFeMnNi high-entropy alloy. *J. Nucl. Mater.* **2019**, *522*, 41–44. [\[CrossRef\]](#)
20. Soundararajan, C.; Luo, H.; Raabe, D.; Li, Z. Hydrogen resistance of a 1 GPa strong equiatomic CoCrNi medium entropy alloy. *Corros. Sci.* **2022**, *167*, 108510. [\[CrossRef\]](#)
21. Zlotea, C.; Sow, M.; Ek, G.; Couzinié, J.; Perrière, L.; Guillot, I.; Bourgon, J.; Möller, K.; Jensen, T.; Akiba, E. Hydrogen sorption in TiZrNbHfTa high entropy alloy. *J. Alloys Compd.* **2019**, *775*, 667–674. [\[CrossRef\]](#)
22. Kim, G.; Lee, S.; Lee, K.; Chun, C.; Lee, J.Y. Observation of the defects induced by hydrogen absorption and desorption in LaNi_5 . *Acta Metall. Mater.* **1995**, *43*, 2233–2240. [\[CrossRef\]](#)
23. Inui, H.; Yamamoto, T.; Hirota, M.; Yamaguchi, M. Lattice defects introduced during hydrogen absorption–desorption cycles and their effects on P–C characteristics in some intermetallic compounds. *J. Alloys Compd.* **2002**, *330*, 117–124. [\[CrossRef\]](#)
24. Zhang, C.; Wu, Y.; You, L.; Cao, X.; Lu, Z.; Song, X. Investigation on the activation mechanism of hydrogen absorption in TiZrNbTa high entropy alloy. *J. Alloys Compd.* **2019**, *781*, 613–620. [\[CrossRef\]](#)
25. Andrade, G.; Zepon, G.; Edalati, K.; Mohammadi, A.; Ma, Z.; Li, H.; Floriano, R. Crystal structure and hydrogen storage properties of AB-type TiZrNbCrFeNi high-entropy alloy. *Int. J. Hydrogen Energy* **2023**, *48*, 13555–13565. [\[CrossRef\]](#)
26. Kumar, A.; Prasad, Y.; Krishna, M. Notable hydrogen storage in Ti–Zr–V–Cr–Ni high entropy alloy. *Int. J. Hydrogen Energy* **2022**, *47*, 22893–22900. [\[CrossRef\]](#)
27. Nygård, M.; Ek, G.; Karlsson, D.; Sahlberg, M.; Sørby, M.; Hauback, B. Hydrogen storage in high-entropy alloys with varying degree of local lattice strain. *Int. J. Hydrogen Energy* **2019**, *44*, 29140–29149. [\[CrossRef\]](#)
28. Kuncce, I.; Polanski, M.; Bystrycki, J. Structure and hydrogen storage properties of a high entropy ZrTiVCrFeNi alloy synthesized using Laser Engineered Net Shaping (LENS). *Int. J. Hydrogen Energy* **2013**, *38*, 12180–12189. [\[CrossRef\]](#)
29. Li, F.; Zhong, B.; Xiao, H.; Ye, X.; Lu, L.; Guan, W.; Zhang, Y.; Wang, X.; Chen, C. Effect of degassing treatment on the deuterium permeability of Pd–Nb–Pd composite membranes during deuterium permeation. *Sep. Purif. Technol.* **2018**, *190*, 136–142. [\[CrossRef\]](#)
30. Phair, J.; Donelson, R. Developments and design of novel (non-palladium-based) metal membranes for hydrogen separation. *Ind. Eng. Chem.* **2006**, *45*, 5657–5674. [\[CrossRef\]](#)
31. Yan, E.; Min, R.; Zhao, P.; Misra, R.; Huang, P.; Zou, Y.; Chu, H.; Zhang, H.; Xu, F.; Sun, L. Design of Nb-based multi-phase alloy membranes for high hydrogen permeability and suppressed hydrogen embrittlement. *J. Membr. Sci.* **2020**, *595*, 117531. [\[CrossRef\]](#)
32. Han, Z.; Liu, X.; Zhao, S.; Shao, Y.; Li, J.; Yao, K. Microstructure, phase stability and mechanical properties of Nb–Ni–Ti–Co–Zr and Nb–Ni–Ti–Co–Zr–Hf high entropy alloys. *Prog. Nat. Sci.* **2015**, *25*, 365–369. [\[CrossRef\]](#)
33. Lundin, C.; Lynch, F.; Magee, C. A correlation between the interstitial hole sizes in intermetallic compounds and the thermodynamic properties of the hydrides formed from those compounds. *J. Less-Common Met.* **1977**, *56*, 19–37. [\[CrossRef\]](#)
34. Fujitani, S.; Yonezu, I.; Saito, T.; Furukawa, N.; Akiba, E.; Hayakawa, H.; Ono, S. Relation between equilibrium hydrogen pressure and lattice parameters in pseudobinary Zr–Mn alloy systems. *J. Less-Common Met.* **1991**, *172*, 220–230. [\[CrossRef\]](#)
35. Cuevas, F.; Joubert, J.; Latroche, M.; Percheron-Guégan, A. Intermetallic compounds as negative electrodes of Ni/MH batteries. *Appl. Phys. A* **2001**, *72*, 225–238. [\[CrossRef\]](#)
36. Galey, B.; Auroux, A.; Sabo-Etienne, S.; Dhaher, S.; Grellier, M.; Postole, G. Improved hydrogen storage properties of Mg/MgH_2 thanks to the addition of nickel hydride complex precursors. *Int. J. Hydrogen Energy* **2019**, *44*, 28848–28862. [\[CrossRef\]](#)
37. Berdonosova, E.; Klyamkin, S.; Zadorozhnyy, V.; Zadorozhnyy, M.; Geodakian, K.; Gorshenkov, M.; Kaloshkin, S. Calorimetric study of peculiar hydrogenation behavior of nanocrystalline TiFe . *J. Alloys Compd.* **2016**, *688*, 1181–1185. [\[CrossRef\]](#)
38. Zadorozhnyy, V.; Berdonosova, E.; Gammer, C.; Eckert, J.; Zadorozhnyy, M.; Bazlov, A.; Klyamkin, S. Mechanochemical synthesis and hydrogenation behavior of $(\text{TiFe})_{100-x}\text{Ni}_x$ alloys. *J. Alloys Compd.* **2019**, *796*, 42–46. [\[CrossRef\]](#)
39. Williams, M.; Lototsky, M.; Davids, M.; Linkov, V.; Yartys, V.; Solberg, J. Chemical surface modification for the improvement of the hydrogenation kinetics and poisoning resistance of TiFe . *J. Alloys Compd.* **2011**, *509*, 770–774. [\[CrossRef\]](#)
40. Somo, T.; Davids, M.; Lototsky, M.; Hato, M.; Modibane, K. Improved hydrogenation kinetics of $\text{TiMn}_{1.52}$ alloy coated with palladium through electroless deposition. *Materials* **2021**, *14*, 1833. [\[CrossRef\]](#)
41. Serov, M. Microcrystalline and amorphous alloys obtained by the method of rapid quenching of melt. *Tekhnol. Legk. Splav.* **2008**, *4*, 34–41.
42. Korol, A.; Zadorozhnyy, V.; Zadorozhnyy, M.; Bazlov, A.; Berdonosova, E.; Serov, M.; Savvotin, I. Production of multi-principal-component alloys by pendent-drop melt extraction. *Int. J. Hydrogen Energy* **2023**, *in press*. [\[CrossRef\]](#)
43. Zadorozhnyy, V.; Tomilin, I.; Berdonosova, E.; Gammer, C.; Zadorozhnyy, M.; Savvotin, I.; Shchetinin, I.; Zheleznyi, M.; Novikov, A.; Bazlov, A.; et al. Composition design, synthesis and hydrogen storage ability of multi-principal-component alloy TiVZrNbTa . *J. Alloys Compd.* **2022**, *901*, 163638. [\[CrossRef\]](#)
44. Sarac, B.; Zadorozhnyy, V.; Ivanov, Y.; Spieckermann, F.; Klyamkin, S.; Berdonosova, E.; Serov, M.; Kaloshkin, S.; Greer, A.; Sarac, A.; et al. Transition metal-based high entropy alloy microfiber electrodes: Corrosion behavior and hydrogen activity. *Corros. Sci.* **2021**, *193*, 109880. [\[CrossRef\]](#)

45. Yakovleva, N.; Ganich, E.; Rumyantseva, T.; Semenenko, K. Interaction mechanism of hydrogen with the CaCu₅-type crystal structure intermetallic compounds. *J. Alloys Compd.* **1996**, *241*, 112–115. [[CrossRef](#)]
46. Shelekhov, E.; Sviridova, T. Programs for X-ray analysis of polycrystals. *J. Met. Sci. Heat Treat.* **2000**, *42*, 309–313. [[CrossRef](#)]
47. Montero, J.; Ek, G.; Laversenne, L.; Nassif, V.; Zepon, G.; Sahlberg, M.; Zlote, C. Hydrogen storage properties of the refractory Ti–V–Zr–Nb–Ta multi-principal element alloy. *J. Alloys Compd.* **2020**, *835*, 155376. [[CrossRef](#)]

Disclaimer/Publisher’s Note: The statements, opinions and data contained in all publications are solely those of the individual author(s) and contributor(s) and not of MDPI and/or the editor(s). MDPI and/or the editor(s) disclaim responsibility for any injury to people or property resulting from any ideas, methods, instructions or products referred to in the content.